Electrical tuning of spin splitting in Bi-doped ZnO nanowires

Mehmet Aras and Çetin Kılıç[*]

Department of Physics, Gebze Technical University, 41400 Gebze Kocaeli, Turkey

The effect of applying an external electric field on doping-induced spin-orbit splitting of the lowest conduction-band states in a bismuth-doped zinc oxide nanowire is studied by performing electronic structure calculations within the framework of density functional theory. It is demonstrated that spin splitting in Bi-doped ZnO nanowires could be tuned and enhanced electrically via control of the strength and direction of the applied electric field, thanks to the nonuniform and anisotropic response of the ZnO:Bi nanowire to external electric fields. The results reported here indicate that a single ZnO nanowire doped with a low concentration of Bi could function as a spintronic device, the operation of which is controlled by applied lateral electric fields.

I. INTRODUCTION

In the presence of noncentrosymmetric electric fields, the spin-orbit (SO) interaction leads to a k-dependent splitting of electronic states, enabling electrical control of the spin-split states in spintronic devices [1–3]. The development of a class of spintronic materials is thus facilitated by engineering (or exploiting) inversion asymmetries to generate *intrinsic* electric fields [4–8] as well as devising architectures in which *external* electric fields are used [9–11]. It has recently been proposed that surface deposition [12] and doping [13] with *heavy* elements could also be used to develop materials with spin-tronic functionalities. In particular, the predictions of Ref. [13] show that doping a *light* semiconducting (ZnO) nanowire with a heavy element (Bi) leads to linear-in-k splitting of the conduction-band (CB) states through SO interaction. It is thus anticipated that a *single* ZnO nanowire doped with a low concentration of Bi could function as a spintronic device.

The objective of the present paper is to investigate if the spintronic properties of a ZnO:Bi nanowire could be tuned or *enhanced* electrically. In our previous paper [13], we showed that the k-dependent SO splitting in ZnO:Bi nanowires could be tuned by adjusting the dopant concentration. Here we demonstrate that applying external electric fields provides an effective means to enhance the linear-in-k SO splitting of the CB states in ZnO:Bi nanowires. We find that the SO splitting energy could be made to have a *superlinear* increase with increasing the electric field strength E, which is mediated by controlling the direction of the applied electric field **E**. This is found to be facilitated by the *nonuniform* and *anisotropic* response of the ZnO:Bi nanowire to external electric fields.

The latter reminds the (converse) piezoelectric response of undoped ZnO nanowires [14–16] and microbelts [17]. On the other hand, our results also indicate that the presence of the substitutional Bi dopant on the ZnO nanowire surface reduces the amount of deformation of the nanowire under an electric field.

As long as single Co-doped ZnO nanowires and nanorods have been produced and characterized [18–20], we think that the realization of a single ZnO:Bi nanowire is *not* beyond the reach of current capabilities, although differences between cobalt and bismuth (e.g., bismuth's larger ionic radius [21] and lower solubility [22] in bulk ZnO) should be taken into consideration. Since experimental studies on single Bi-doped ZnO nanowires were not available (to our knowledge), the realization and stability of a single ZnO:Bi nanowire were examined theoretically in our previous publications [13,23] with the aid of *defect* calculations and finite-temperature *ab initio* molecular dynamics simulations, as discussed in the Appendix.

II. COMPUTATIONAL DETAILS

The findings reported here were obtained via electronic structure calculations performed within the framework of the density functional theory (DFT) by employing periodic supercells. Although the supercells were in practice subject to the Bloch periodicity condition in all directions, the supercell dimensions perpendicular to the nanowire axis were set to be significantly larger than the nanowire diameter in order to create a vacuum region (of thickness larger than 15 Å) that avoid interactions between the nanowire and its periodic images. We used the Vienna *ab initio* simulation package [24] (VASP) together with its projected-augmented-wave potential database [25], adopting the rotationally-invariant DFT + U approach [26] in combination with the Perdew-Burke-Ernzerhof exchange-correlation functional [27], and taking the SO coupling into account as implemented [28,29] in the VASP code. The $2s$ and $2p$, $3d$ and $4s$, and $6s$ and $6p$ states were treated as valence states for oxygen, zinc, and bismuth, respectively. Plane-wave basis sets with a kinetic energy cutoff of 400 eV were used to represent the electronic states. In test calculations [13] the kinetic energy cutoff was increased by 10% and the change in the SO splitting energies turned out to be smaller than 0.5%. The value of Hubbard U was set to 7.7 eV [23], which was applied to the Zn $3d$ states. The DFT + U approach was preferred over the standard (semilocal) DFT calculations

———————
[*]cetin_kilic@gtu.edu.tr

in order to reduce the underestimation of the d-state binding energies [30]. We applied *lateral* electric fields in the x or y direction of varying strength E (from 0.1 to 0.5 eV/Å with an increment of 0.1 eV/Å), orienting the nanowire axis along the z direction. It should be noted that VASP handles the external electric fields by introducing artificial dipole sheets in the middle of the vacuum regions in the supercell (cf. Ref. [31]).

Structural optimizations were performed for each atomic configuration, separately for each given **E**, by minimizing the total energy until the maximum value of residual forces on atoms was reduced to be smaller than 10^{-2} eV/Å, using the Γ point for sampling the supercell Brillouin zone (BZ). We determined [13] an error bar of 0.2 meV for the energy per ZnO unit owing to the BZ sampling achieved through zone folding. Convergence criterion for the electronic self-consistency was set up to 10^{-6} and 10^{-8} eV in structural optimizations and electronic structure calculations, respectively.

III. RESULTS AND DISCUSSION

Figure 1(a) shows the equilibrium atomic configuration for a Bi-doped ZnO nanowire in the absence of an external electric field, where the Bi dopant substitutes Zn at a surface site of the host ZnO nanowire. We refer the reader to the Appendix for a discussion of issues concerning the realization of this configuration. The equilibrium atomic configuration for the undoped (host) nanowire is also shown in Fig. 1(a), which was used in former theoretical studies by others (e.g., Refs. [15,32]) as well as the authors [13,23]. The wire thicknesses t_x and t_y are indicated in Fig. 1(a) for both the doped and the undoped nanowires. Comparing these thicknesses, it is clear that the incorporation of Bi causes insignificant deformation in the wire morphology, which means that the accommodation of Bi induces mostly local relaxations. It should also be pointed out that the host nanowire's thickness is smaller than the experimental diameter (D) values measured for high-aspect-ratio ZnO nanorods with $D \geqslant 2.2$ nm [33] and thin ZnO nanowires with $D \geqslant 4.1$ nm [34]. The variation of the results with respect to the nanowire's thickness was studied in Ref. [13] (in the absence of an external electric field), which is not done here.

The equilibrium configurations in the presence of electric fields are given in Figs. 1(b) and S1 (see Ref. [35]). Since the electric-field-induced changes in the atomic positions are not visible in the scale of the figures, the sticks representing the Zn-O bonds are colored to reflect the electric-field-induced changes Δd in the bond lengths. Hence, the structural response of the ZnO:Bi nanowire to the applied electric fields could be inferred from the distributions of red and green sticks (representing the elongated and shrunk bonds, respectively). It is clear in Figs. 1(b) and S1 (see Ref. [35]) that the electric-field-induced structural changes occur all around the nanowire. Nevertheless, a comparison between the bond lengths in Regions I and II depicted in Fig. 1(a), the values of which are provided in Table S1 (see Ref. [35]), reveals that the structural changes are more pronounced in the vicinity of the dopant. For example, the O1-Bi (O2-Bi) bond located in Region I exhibits the greatest shrinkage for $\mathbf{E}/\!/\hat{\mathbf{x}}$ ($\mathbf{E}/\!/\hat{\mathbf{y}}$), the degree of which is proportional to E. The respective bonds in Region II (far from the dopant), i.e., the O4-Zn7 and O5-Zn7 bonds, however, exhibit considerably smaller shrinkage.
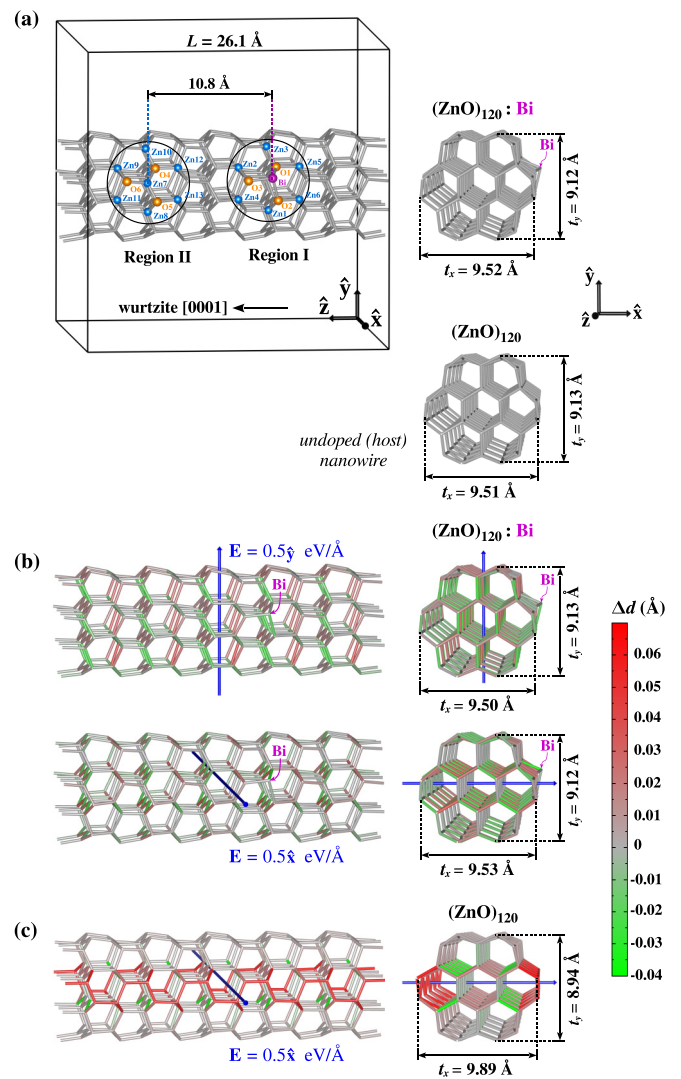

FIG. 1. The equilibrium atomic configuration for the Bi-doped nanowire (a) in the absence of an external electric field and (b) for $\mathbf{E} = 0.5\hat{\mathbf{y}}$ and $\mathbf{E} = 0.5\hat{\mathbf{x}}$ eV/Å. (c) The same for the undoped (i.e., host) nanowire for $\mathbf{E} = 0.5\hat{\mathbf{x}}$ eV/Å. The host nanowire for $\mathbf{E} = \mathbf{0}$ is also included in panel (a). The sticks in panels (b) and (c) representing the Zn-O bonds are colored to reflect the electric-field-induced changes Δd in the bond lengths. The thicknesses t_x and t_y are indicated.

As mentioned above, the presence of the Bi dopant on the ZnO nanowire surface reduces the amount of deformation in the wire morphology under a lateral electric field. This could be seen by comparing the structures in Figs. 1(b) and 1(c). For the doped nanowire, the t_x and t_y values in Fig. 1(b) are *little* different from those in Fig. 1(a). In contrast, there is a *significant* increase (decrease) in the t_x (t_y) of the undoped nanowire as a result of applying $\mathbf{E} = 0.5\hat{\mathbf{x}}$ eV/Å, yielding a noticeable modification in the wire cross-section since the ratio t_x/t_y changes from 1.04 to 1.11. The distribution of the stretched (shrunk) bonds, cf. red (green) sticks, in Fig. 1(c) is also noticeably different than that in Fig. 1(b), which reveals the microscopic origin of the increase (decrease) in t_x (t_y). It should be noticed that applying a lateral electric field makes the Zn-O bonds that are aligned with the wire axis elongate
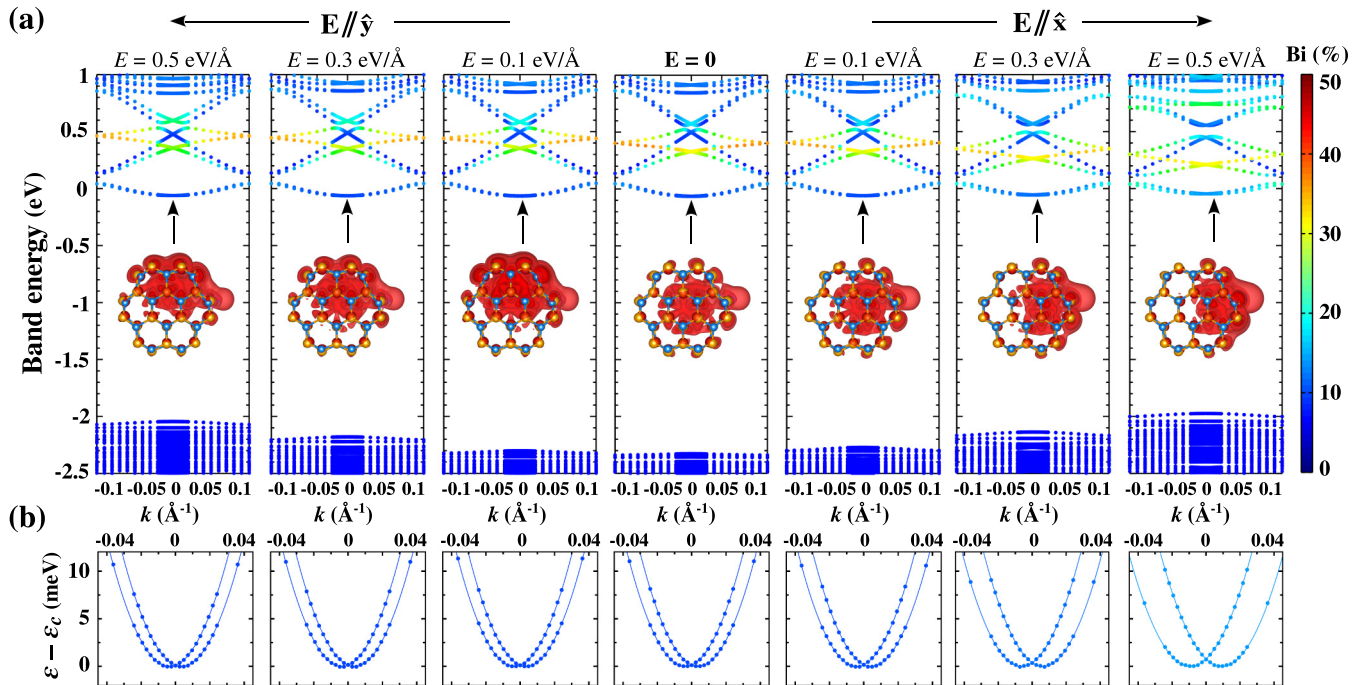
FIG. 2. (a) The electronic energy bands of the $(ZnO)_{120}$:Bi nanowire under applied electric fields, which are colored to reflect the percent contribution from Bi to the electronic states. The Fermi level is set as the zero of energy. The vertical arrows point to the CBM. The red isosurfaces in the insets of the upper panels represent the CBM state charge densities for the isovalue of 1×10^{-4} Å^{-3}. (b) Close-up views showing the spin-orbit splitting of the *two* lowest conduction bands.

according to our prediction, which is in accordance with the response of a ZnO microbelt [17] to an applied electric field perpendicular to its c axis.

The electronic energy bands of the $(ZnO)_{120}$:Bi nanowire, calculated for $\mathbf{E} = 0.5\hat{y}$, $0.4\hat{y}$, $0.3\hat{y}$, $0.2\hat{y}$, $0.1\hat{y}$, $\mathbf{0}$, $0.1\hat{x}$, $0.2\hat{x}$, $0.3\hat{x}$, $0.4\hat{x}$, and $0.5\hat{x}$ eV/Å, are shown in Figs. 2(a) and S2(a) (see Ref. [35]) where the symbols are colored to reflect the percent contribution from Bi to the electronic states. The coloring is accomplished by computing the contributions from the Zn, O, and Bi atoms that are obtained by projecting the state wave functions onto spherical harmonics within a sphere around each atom. The vertical arrows point to the conduction-band minimum (CBM) that occurs at $k = k_c$. It is seen that Bi-derived states occur as resonances in the conduction band, energies of which get lowered (remain roughly constant) for $\mathbf{E} // \hat{x}$ ($\mathbf{E} // \hat{y}$). The CBM state charge density $\rho_\mathbf{E}(\mathbf{r}) = |\psi_\mathbf{E}(\mathbf{r})|^2$ is noticeably distorted *in a directed manner* as imposed by the direction of the applied electric field $\mathbf{E}$, which is inferred from the isosurfaces given as insets in Fig. 2(a). Whereas the Bi contribution to the CBM wave function $\psi_\mathbf{E}$ decreases slowly with E for $\mathbf{E} // \hat{y}$, applying $\mathbf{E}$ in the x direction makes the CBM wave function have a higher contribution from Bi, in proportionality with E. Thus an important effect of applying an external electric field is to vary the Bi contribution to the lower CB states.

Figures 2(b) and S2(b) (see Ref. [35]) display close-up views of the *two* lowest (spin-split) conduction bands, where the bands are shifted by subtracting the lowest eigenvalue ε_c of the conduction band from the band energies ε. These bands are partially occupied since the aforementioned Bi-derived resonant states in the conduction band are empty, reflecting the

donor behavior of Bi in ZnO nanowires [23]. The dispersion of the spin-split bands in Fig. 2(b) is *accurately* described by

$$\varepsilon_\pm(k) = \frac{\hbar^2}{2m^*}k^2 \pm \alpha k, \tag{1}$$

represented by the solid curves in each panel. Although Eq. (1) is of the same form of the Bychkov-Rashba expression [36], the electrons filling the $\varepsilon_\pm$ bands do *not* form a two-dimensional electron gas, as seen from the insets of Figs. 2(a) and S2(a) (see Ref. [35]). The latter applies to the case of *zero* electric field, as discussed in detail in Ref. [13]. It is clear that the splitting energy $\Delta\varepsilon(k) = \varepsilon_+(k) - \varepsilon_-(k)$ increases (decreases slowly) as E increases for $\mathbf{E} // \hat{x}$ ($\mathbf{E} // \hat{y}$). This is the same trend for the Bi contribution to the CBM wave function, as noted in the preceding paragraph. Accordingly the variations of $\Delta\varepsilon(k_c)$ and the Bi contribution to $\psi_\mathbf{E}$ with E follow the same trend, as seen in Figs. 3(a) and 3(b). This means that increasing the Bi contribution to the lower CB states leads to the enhancement of spin-orbit splitting of those states. It should also be pointed out that $\mathbf{E}$ induces a *much smaller* splitting in the *undoped* nanowire owing to the absence of the Bi contribution. This is illustrated in Fig. S3 (see Ref. [35]) where the linear coefficient $\alpha = 0.02$ eV Å in the absence of the heavy element Bi, which should be compared to the respective value of $\alpha = 0.17$ eV Å in the presence of the Bi dopant.

The splitting energy plotted in Fig. 3(a) is given by $\Delta\varepsilon(k_c) = 2\alpha k_c$ according to Eq. (1). Thus the variation of the linear coefficient α and the momentum offset k_c with $\mathbf{E}$ is studied in Figs. 3(c) and 3(d), respectively, where the black curves
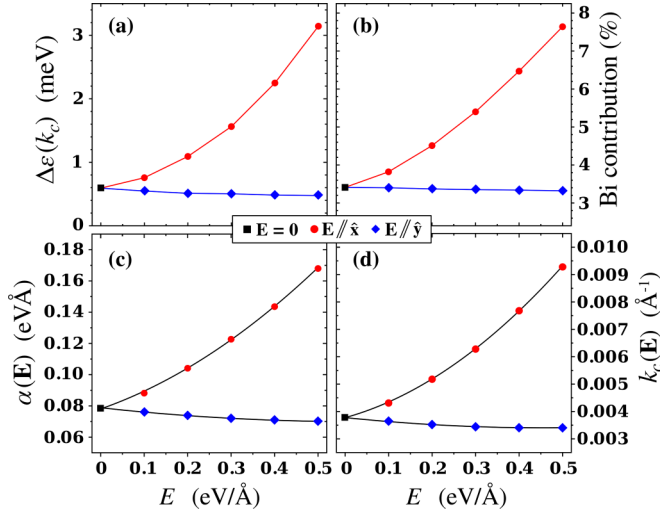
FIG. 3. The variation of the (a) splitting energy $\Delta\varepsilon(k_c)$, (b) Bi contribution to the CBM wave function, (c) linear coefficient α, and (d) momentum offset k_c with the external electric field strength E.

represent the parametrization according to

$$\alpha(\mathbf{E}) = \begin{cases} \alpha_0 + 0.097E + 0.168E^2 & \text{if } \mathbf{E} /\!/ \hat{\mathbf{x}} \\ \alpha_0 - 0.030E + 0.026E^2 & \text{if } \mathbf{E} /\!/ \hat{\mathbf{y}}, \end{cases} \quad (2)$$

$$k_c(\mathbf{E}) = \begin{cases} k_0 + 0.0044E + 0.0134E^2 & \text{if } \mathbf{E} /\!/ \hat{\mathbf{x}} \\ k_0 - 0.0016E + 0.0179E^2 & \text{if } \mathbf{E} /\!/ \hat{\mathbf{y}}. \end{cases} \quad (3)$$

Here the units of α, k_c, and E are eV Å, Å^{-1}, and eV/Å, respectively; $\alpha_0 = \alpha(\mathbf{0}) = 0.079$ eV Å and $k_0 = k_c(\mathbf{0}) = 0.0038$ Å^{-1} are the values of the linear coefficient and the momentum offset, respectively, in the absence of an external electric field. It is noteworthy that $\alpha(\mathbf{E})$ and $k_c(\mathbf{E})$ are both substantially enhanced with increasing E in the case of $\mathbf{E} /\!/ \hat{\mathbf{x}}$, whereas they exhibit a slight decrease for $\mathbf{E} /\!/ \hat{\mathbf{y}}$. The variation of $\alpha(\mathbf{E})$ with E is seemingly *superlinear* for $\mathbf{E} /\!/ \hat{\mathbf{x}}$. It is also notable that the (ZnO)$_{120}$:Bi nanowire has an *anisotropic* response to the external electric fields as regards the degree of SO splitting of CB states. Thus, in an experimental setup, it would be necessary first to determine the electric field directions for which $\alpha(\mathbf{E})$ and $k_c(\mathbf{E})$ show increasing and decreasing variations with increasing E. This would enable directional control of the spin-split states in a practical application.

From a fundamental physics point of view, the linear coefficient α introduced in Eq. (1) is related to the expectation value of the SO interaction operator H_{SO} with $\psi_{\mathbf{E}}(\mathbf{r})$, which could be approximated [13] as $\langle H_{\text{SO}} \rangle = -\langle \mathbf{m} \rangle \cdot \langle \mathbf{B}_{\text{SO}} \rangle$, where $\langle \mathbf{m} \rangle$ and $\langle \mathbf{B}_{\text{SO}} \rangle$ denote the expectation values of the magnetization density $\mathbf{m}(\mathbf{r})$ and the operator $\mathbf{B}_{\text{SO}} = -[(\vec{\nabla} V - e\mathbf{E}) \times \mathbf{p}]/2emc^2$, respectively. A linear dependence of $\alpha(\mathbf{E})$ on $\mathbf{E}$ would therefore be expected. Hence the nonlinear variation $\alpha(\mathbf{E})$ with the applied electric field in Fig. 3(c) deserves further investigation. To this aim, the variation of $\alpha(\mathbf{E})$ with $\mathbf{E}$ is analyzed in terms of $\mathbf{E}$-induced changes in $\langle \mathbf{m} \rangle$ and $\langle \mathbf{B}_{\text{SO}} \rangle$. Note that not only $\langle \mathbf{B}_{\text{SO}} \rangle$ but also $\langle \mathbf{m} \rangle$ varies with $\mathbf{E}$ in our noncollinear DFT calculations where $\mathbf{m}(\mathbf{r})$ is determined self-consistently, as shown in Fig. 4(a) where φ denotes the angle between $\mathbf{E}$ and $\langle \mathbf{m} \rangle$. The computed values for the magnitude of $\langle \mathbf{m} \rangle$ are given in Table S2
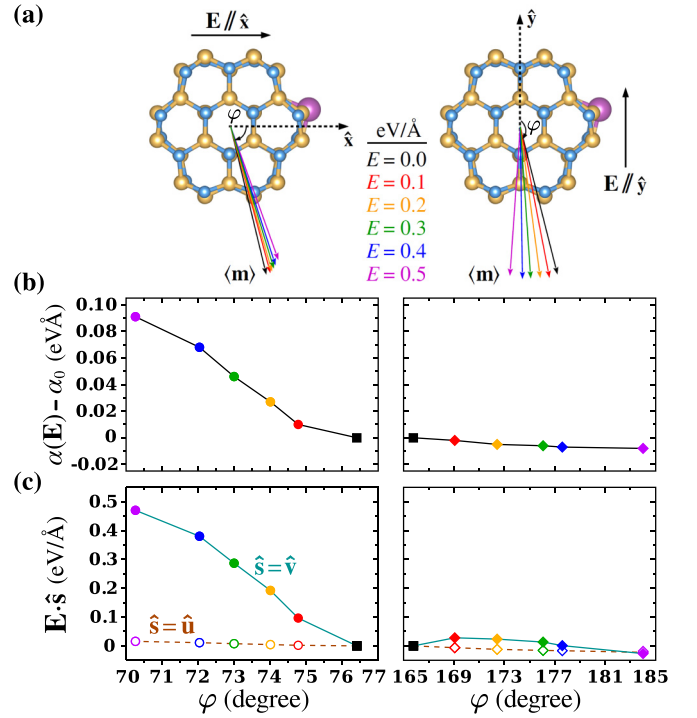

FIG. 4. (a) The expectation value $\langle \mathbf{m} \rangle$ of the magnetization density with the CBM wave function for $\mathbf{E} /\!/ \hat{\mathbf{x}}$ and $\mathbf{E} /\!/ \hat{\mathbf{y}}$. The plots of (b) the plots of the electric-field-induced change in α and (c) the projections $\mathbf{E} \cdot \hat{\mathbf{s}}$ ($\hat{\mathbf{s}} = \hat{\mathbf{u}}$ and $\hat{\mathbf{v}}$) with $\hat{\mathbf{s}} \perp \langle \mathbf{m} \rangle$ versus the angle φ between $\mathbf{E}$ and $\langle \mathbf{m} \rangle$.

(see Ref. [35]). It should also be noted that the projections of the vector $\mathbf{E}$ *perpendicular (parallel)* to the vector $\langle \mathbf{m} \rangle$ make *nonzero (zero)* contributions to $\langle H_{\text{SO}} \rangle$, and therefore to the splitting energy. It is thus convenient to use an intrinsic coordinate system defined by the orthogonal unit vectors $\hat{\mathbf{u}}$, $\hat{\mathbf{v}}$, and $\hat{\mathbf{w}}$ satisfying $\hat{\mathbf{w}} /\!/ \langle \mathbf{m} \rangle$ and $\hat{\mathbf{u}}, \hat{\mathbf{v}} \perp \langle \mathbf{m} \rangle$, which could be taken as $\hat{\mathbf{u}} = \cos\theta\cos\phi\hat{\mathbf{x}} + \cos\theta\sin\phi\hat{\mathbf{y}} - \sin\theta\hat{\mathbf{z}}$, $\hat{\mathbf{v}} = -\sin\phi\hat{\mathbf{x}} + \cos\phi\hat{\mathbf{y}}$, and $\hat{\mathbf{w}} = \sin\theta\cos\phi\hat{\mathbf{x}} + \sin\theta\sin\phi\hat{\mathbf{y}} + \cos\theta\hat{\mathbf{z}}$, where θ and ϕ denote the angles between $\langle \mathbf{m} \rangle$ and $\hat{\mathbf{z}}$ and $\langle \mathbf{m} \rangle$ and $\hat{\mathbf{x}}$, respectively. For the $\langle \mathbf{m} \rangle$ vectors in Fig. 4(a), the angle pairs (θ, ϕ) take the values given in Table S2 (see Ref. [35]). It is important to notice that the electric-field-induced change in $\langle \mathbf{B}_{\text{SO}} \rangle$ arising *only* from the projections $\mathbf{E} \cdot \hat{\mathbf{s}}$ with $\hat{\mathbf{s}} \neq \hat{\mathbf{w}}$ yields a *nonzero* contribution to $\langle H_{\text{SO}} \rangle$. It is thus instructive to explore the relationship between the $\mathbf{E}$-induced variation of α, i.e., $\Delta\alpha = \alpha(\mathbf{E}) - \alpha_0$, and the projections $\mathbf{E} \cdot \hat{\mathbf{s}}$ with $\hat{\mathbf{s}} = \hat{\mathbf{u}}$ and $\hat{\mathbf{v}}$ as well as the $\mathbf{E}$-induced change in $\langle \mathbf{m} \rangle$, which is denoted as $\Delta\langle \mathbf{m} \rangle$. A comparative inspection of Figs. 4(b) and 4(c) reveals that the variation of $\Delta\alpha$ with respect to φ is of the same trend as that of $\mathbf{E} \cdot \hat{\mathbf{v}}$ ($\mathbf{E} \cdot \hat{\mathbf{u}}$) for $\mathbf{E} /\!/ \hat{\mathbf{x}}$ ($\mathbf{E} /\!/ \hat{\mathbf{y}}$). In view of this and the foregoing discussion, a fitting according to

$$\Delta\alpha = c_u \mathbf{E} \cdot \hat{\mathbf{u}} + c_v \mathbf{E} \cdot \hat{\mathbf{v}} + c_m \Delta\langle \mathbf{m} \rangle \cdot \hat{\mathbf{w}}_0 \quad (4)$$

was performed, where $\hat{\mathbf{w}}_0$ denotes the unit vector in the direction of $\langle \mathbf{m} \rangle$ in the *absence* of the external electric field. We found that the result of this fitting is *not* entirely satisfactory, which was inferred from Fig. 5(a). We attribute the latter to the fact that the *nonuniform* response of the nanowire to the applied electric field is *not* taken into account in Eq. (4),
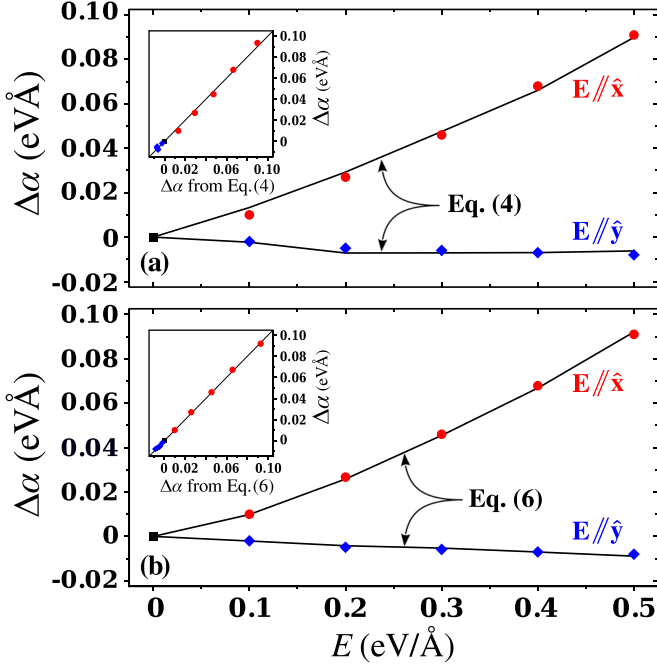
FIG. 5. The plots of the electric-field-induced change $\Delta\alpha$ in α versus the electric field strength E for $\mathbf{E} \parallel \hat{\mathbf{x}}$ (the red circles) and $\mathbf{E} \parallel \hat{\mathbf{y}}$ (the blue diamonds). The black curves represent the result of fitting according to (a) Eq. (4) and (b) Eq. (6). The insets show the plots of the original $\Delta\alpha$ values versus the $\Delta\alpha$ values obtained from (a) Eq. (4) and (b) Eq. (6).

which is demonstrated by the graphs of the $\mathbf{E}$-induced change $\Delta\rho(\mathbf{r}) = \rho_E(\mathbf{r}) - \rho_0(\mathbf{r})$ in the CBM state charge density in Fig. 6. The projections $\mathbf{E} \cdot \hat{\mathbf{s}}$ in Eq. (4) are thus replaced by the integrals

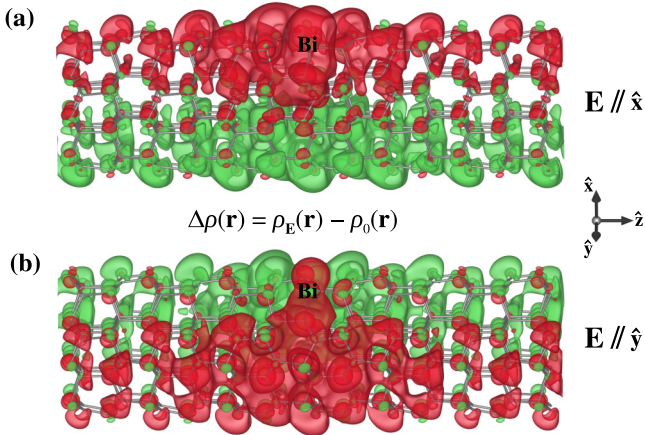$$I_s = \int -\vec{\nabla}[\Delta V(\mathbf{r})] \cdot \hat{\mathbf{s}}\rho_E(\mathbf{r})d^3r, \qquad (5)$$

FIG. 6. The isosurfaces of $\Delta\rho(\mathbf{r})$ with isovalues of $\pm 5 \times 10^{-5}$ Å^{-3} for (a) $\mathbf{E} = 0.5\hat{\mathbf{x}}$ eV/Å and (b) $\mathbf{E} = 0.5\hat{\mathbf{y}}$ eV/Å. The CBM state is polarized as imposed by the direction of the applied electric field since the red and green isosurfaces represent electric-field-induced increase and decrease in the CBM state charge density, respectively.

TABLE I. First and second columns: The electric-field-induced change in the linear coefficient α computed from $\Delta\alpha = \alpha(\mathbf{E}) - \alpha_0$ and Eq. (6), respectively. Third, fourth, and fifth columns: The contributions to $\Delta\alpha$ from the RHS terms of Eq. (6). All values are in eV Å.

$\Delta\alpha$	RHS of Eq. (6)	$c_u I_u$	$c_v I_v$	$c_m \Delta\langle\mathbf{m}\rangle \cdot \hat{\mathbf{w}}_0$
−0.008	−0.009	−0.0145	−0.0035	0.0091
−0.007	−0.007	−0.0114	0.0001	0.0043
−0.006	−0.006	−0.0097	0.0015	0.0030
−0.005	−0.004	−0.0074	0.0026	0.0006
−0.002	−0.002	−0.0040	0.0018	0.0001
0.010	0.009	0.0014	0.0083	0.0002
0.027	0.026	0.0028	0.0213	0.0017
0.046	0.046	0.0048	0.0367	0.0040
0.068	0.067	0.0070	0.0522	0.0067
0.091	0.092	0.0100	0.0718	0.0113

with $s = u$ or v, resulting in

$$\Delta\alpha = c_u I_u + c_v I_v + c_m \Delta\langle\mathbf{m}\rangle \cdot \hat{\mathbf{w}}_0. \qquad (6)$$

In Eq. (5), $\Delta V(\mathbf{r})$ denotes the electric-field-induced change in the *self-consistent* potential $V(\mathbf{r})$. Note that $I_s = \mathbf{E} \cdot \hat{\mathbf{s}}$ for a *uniform* electric field within a *non-self-consistent* description. The fitting according to Eq. (6) yields $c_u = 1.7464$ Å^2, $c_v = 0.3525$ Å^2, and $c_m = -0.3212$ eVÅ/μ_B, the result of which is quite satisfactory as seen in Fig. 5(b). The $\Delta\alpha$ values obtained from the right-hand-side (RHS) of Eq. (6) are given in the second column of Table I, which should be compared to the original values in the first column of the same table. The contributions from the three terms in the RHS of Eq. (6) are given in the third, fourth, and fifth columns of Table I. It is noticeable that the $c_u I_u$ and $c_v I_v$ terms have the greatest contribution to $\Delta\alpha$ for $\Delta\alpha < 0$ and $\Delta\alpha > 0$, respectively, although the $c_m \Delta\langle\mathbf{m}\rangle \cdot \hat{\mathbf{w}}_0$ term has also a non-negligible contribution. Since both c_u and c_v are *positive*, a decrease in α occurs owing to $I_u < 0$ when $\mathbf{E} \parallel \hat{\mathbf{y}}$. On the other hand, an increase in α occurs when $I_v > 0$ and/or $I_u > 0$. Hence the increasing and decreasing variation of α with $\mathbf{E}$ is traced to the *sign* of the I_s ($s = u$ and v) integrals, which is practically the same as the sign of $\mathbf{E} \cdot \hat{\mathbf{s}}$. Accordingly, as long as the directions $\hat{\mathbf{u}}$ and $\hat{\mathbf{v}}$ can *not* be determined *a priori*, the direction of the applied electric field must be chosen carefully to ensure that an electric-field-induced *increase* in α is achieved. The latter would facilitate the directional control of the spin-split CB states, as also mentioned above, which would likely involve trial-and-error in a practical application. It is nonetheless remarkable that a *single* ZnO:Bi nanowire such as that studied here can function as a spintronic device, the operation of which is controlled by applying lateral electric fields.

IV. CONCLUSION

In summary, the results of our density functional calculations show that doping-induced linear-in-k spin splitting of the lowest conduction-band states in a Bi-doped ZnO nanowire can be tuned by applying lateral electric fields via control of

the electric field strength and direction. We find that the degree of this splitting can be made to have a superlinear increase with increasing electric field strength, which is mediated by controlling the electric field direction. Our analysis reveals that this is facilitated by the nonuniform and anisotropic response of the ZnO:Bi nanowire to the applied electric field. These findings indicate that a single ZnO nanowire doped with a low concentration of Bi can function as a spintronic device, the operation of which is controlled electrically.

APPENDIX: Bi DEFECTS IN THE ZnO:Bi NANOWIRE

We have recently conducted [23] a theoretical characterization of a Bi-doped ZnO nanowire in a site-specific manner as regards the location and charge-state of the dopant, by calculating the defect formation energy ΔH_f for a number of extrinsic defects formed via the incorporation of Bi into the Zn, O, or interstitial (i) sites in the bulklike (b), surface (s), or subsurface (ss) regions of the nanowire. It is to be emphasized that ΔH_f is an indicator for the *abundance* of the defect under given thermodynamic conditions since it is a significant portion of the *Gibbs energy of formation* that determines the *equilibrium defect concentration*. The defects considered are shown in the inset of Fig. 7, which are denoted as $\mathrm{Bi_{Zn}}(b)$, $\mathrm{Bi_O}(b)$, $\mathrm{Bi}_i(b)$, $\mathrm{Bi_{Zn}}(ss)$, $\mathrm{Bi_O}(ss)$, $\mathrm{Bi_{Zn}}(s)$, and $\mathrm{Bi_O}(s)$. In structural optimizations, placing Bi initially at either of the *unlabeled* sites shown in the inset of Fig. 7 resulted in an *unstable* configuration in which the nanowire was damaged. These two unstable configurations were discarded. In the present paper, the doping configuration displayed in Fig. 1(a) contains the defect $\mathrm{Bi_{Zn}}(s)$. We studied the formation energies of the foregoing defects as a function of the Fermi level ε_F and the atomic chemical potentials μ_Zn, μ_O, and μ_Bi. Our investigations [13,23] indicate that this doping configuration can be realized under reasonable thermodynamic conditions, which are summarized here with the aid of the plots of ΔH_f versus the difference $\mu_\mathrm{O} - \mu_\mathrm{Zn}$. The latter are given in Figs. 7(a) and 7(b) for *two* limiting values of ε_F. The value of μ_Bi is set to the adsorption energy of a Bi atom on the nanowire surface (cf. Ref. [13]). It is seen in Figs. 7(a) and 7(b) that the defect $\mathrm{Bi_{Zn}}(s)$ in the charge state 0 or + (depending on the location of the Fermi level) has not only the *lowest* but also *negative* formation energies for a wide range of thermodynamic conditions. The only exception to this is that $\mathrm{Bi_O}(s)$ has a lower formation energy under O-poor conditions for $\varepsilon_\mathrm{F} = \varepsilon_c$ in a narrow range of $\mu_\mathrm{O} - \mu_\mathrm{Zn}$. Clearly, the formation of $\mathrm{Bi_{Zn}}(s)$, rather than the rest of the alternatives with *higher* formation energies, could be favored by adjusting thermodynamic conditions (i.e., by avoiding the values of μ_O and μ_Zn corresponding to the latter range of $\mu_\mathrm{O} - \mu_\mathrm{Zn}$). This means that the doping configuration displayed
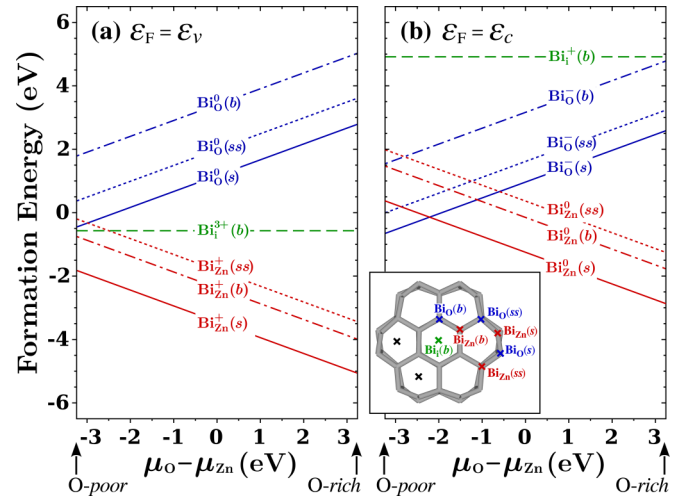

FIG. 7. The formation energies of the extrinsic defects formed via the incorporation of Bi into the Zn, O, or interstitial (i) sites in the bulklike (b), surface (s), or subsurface (ss) regions of the ZnO nanowire, as shown in the inset, are plotted as a function of the difference $\mu_\mathrm{O} - \mu_\mathrm{Zn}$ for (a) $\varepsilon_\mathrm{F} = \varepsilon_v$ and (b) $\varepsilon_\mathrm{F} = \varepsilon_c$, where ε_v and ε_c denote the highest and lowest eigenvalues of the valence and conduction bands, respectively. The limiting values of $\mu_\mathrm{O} - \mu_\mathrm{Zn}$ corresponding to O-poor (i.e., Zn-rich) and O-rich (i.e., Zn-poor) conditions are indicated by the vertical arrows. In the inset, the black crosses represent the *unlabeled* sites corresponding to the two discarded (unstable) configurations.
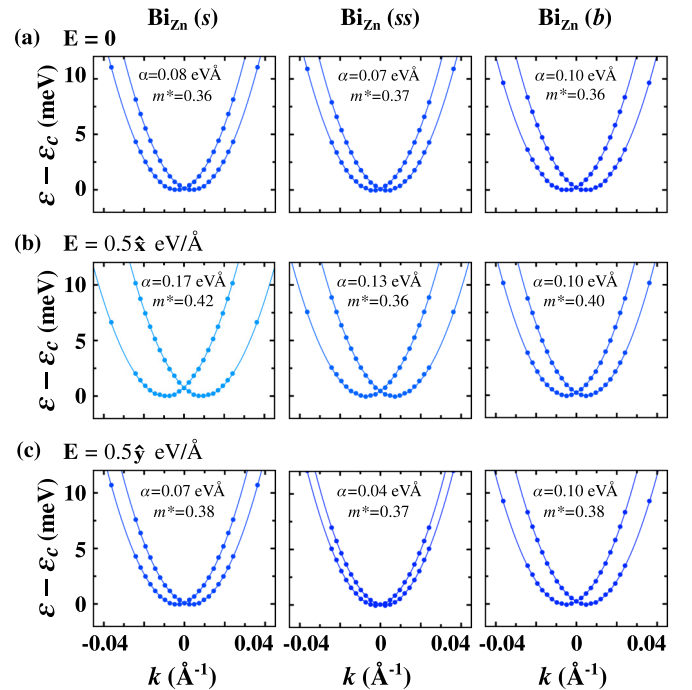

FIG. 8. Spin-split conduction bands for ZnO:Bi nanowires containing $\mathrm{Bi_{Zn}}(s)$, $\mathrm{Bi_{Zn}}(ss)$, and $\mathrm{Bi_{Zn}}(b)$ for (a) $\mathbf{E} = \mathbf{0}$, (b) $\mathbf{E} = 0.5\hat{\mathbf{x}}$ eV/Å, and (c) $\mathbf{E} = 0.5\hat{\mathbf{y}}$ eV/Å. The values of the linear coefficient α (in eV Å) and the effective mass m^* (in free-electron mass) are given in each panel.

in Fig. 1(a) could be realized under controlled thermodynamic conditions. Besides, *ab initio* molecular dynamics simulations performed at high temperature indicate that the same degree of stability could be assigned to the undoped ZnO and doped ZnO:Bi nanowires [13]. Finally, we think that the synthesis of surface-doped ZnO:Bi nanowire studied here would benefit from the low solubility of Bi in ZnO that derives the *segregation* of Bi in ZnO varistors [22,37]. A segregation tendency is also revealed for Bi in ZnO nanowires in Figs. 7(a) and 7(b) where the surface (*s*) defects have lower formation energies compared to the respective bulklike (*b*) and subsurface (*ss*) defects.

Since the formation energy of $Bi_{Zn}(s)$ is significantly lower than that of $Bi_{Zn}(ss)$ and $Bi_{Zn}(b)$, cf. Figs. 7(a) and 7(b), the equilibrium concentration of $Bi_{Zn}(s)$ would be *several orders of magnitude higher* than that of $Bi_{Zn}(ss)$ and $Bi_{Zn}(b)$

at room temperature. It is nevertheless interesting to see if spin splitting of the CB states occurs also for $Bi_{Zn}(ss)$ and $Bi_{Zn}(b)$. Figures 8(a)–8(c) show the SO-split conduction bands for ZnO:Bi nanowires containing $Bi_{Zn}(s)$, $Bi_{Zn}(ss)$, and $Bi_{Zn}(b)$ for $\mathbf{E} = \mathbf{0}$, $0.5\hat{\mathbf{x}}$, and $0.5\hat{\mathbf{y}}$ eV/Å. An expanded view of the band structures are provided in Fig. S4 (see Ref. [35]) where the optimized atomic structures are included as insets. Note that spin-orbit splitting of the CB states is present in each panel of Fig. 8. Moreover, the linear coefficient α takes quite similar values for $Bi_{Zn}(s)$, $Bi_{Zn}(ss)$, and $Bi_{Zn}(b)$. On the other hand, α for $Bi_{Zn}(b)$ does not show much variation with $\mathbf{E}$. The latter implies that electrical control of doping-induced spin splitting explored here could be achieved only in the case of surface (as opposed to bulk) doping of ZnO nanowires with Bi.

[1] E. I. Rashba and A. L. Efros, Phys. Rev. Lett. **91**, 126405 (2003).

[2] S. Sahoo, T. Kontos, J. Furer, C. Hoffmann, M. Graber, A. Cottet, and C. Schonenberger, Nat. Phys. **1**, 99 (2005).

[3] K. C. Nowack, F. H. L. Koppens, Y. V. Nazarov, and L. M. K. Vandersypen, Science **318**, 1430 (2007).

[4] K. Ishizaka *et al.*, Nat. Mater. **10**, 521 (2011).

[5] D. Di Sante, P. Barone, R. Bertacco, and S. Picozzi, Adv. Mater. **25**, 509 (2013).

[6] Q. Liu, Y. Guo, and A. J. Freeman, Nano Lett. **13**, 5264 (2013).

[7] S. Güler-Kılıç and Ç. Kılıç, Phys. Rev. B **91**, 245204 (2015).

[8] C. Cheng, J.-T. Sun, X.-R. Chen, H.-X. Fu, and S. Meng, Nanoscale **8**, 17854 (2016).

[9] J. Nitta, T. Akazaki, H. Takayanagi, and T. Enoki, Phys. Rev. Lett. **78**, 1335 (1997).

[10] D. Liang and X. P. Gao, Nano Lett. **12**, 3263 (2012).

[11] S.-J. Gong, C.-G. Duan, Y. Zhu, Z.-Q. Zhu, and J.-H. Chu, Phys. Rev. B **87**, 035403 (2013).

[12] F. Calleja, H. Ochoa, M. Garnica, S. Barja, J. J. Navarro, A. Black, M. M. Otrokov, E. V. Chulkov, A. Arnau, A. L. Vazquez de Parga, F. Guinea, and R. Miranda, Nat. Phys. **11**, 43 (2014).

[13] M. Aras, S. Güler-Kılıç, and Ç. Kılıç, Phys. Rev. B **95**, 155404 (2017).

[14] J. H. He, C. L. Hsin, J. Liu, L. J. Chen, and Z. L. Wang, Adv. Mater. **19**, 781 (2007).

[15] R. Agrawal and H. D. Espinosa, Nano Lett. **11**, 786 (2011).

[16] E. Broitman, M. Y. Soomro, J. Lu, M. Willander, and L. Hultman, Phys. Chem. Chem. Phys. **15**, 11113 (2013).

[17] Y. Hu, Y. Gao, S. Singamaneni, V. V. Tsukruk, and Z. L. Wang, Nano Lett. **9**, 2661 (2009).

[18] W. Liang, B. D. Yuhas, and P. Yang, Nano Lett. **9**, 892 (2009).

[19] J. Segura-Ruiz, G. Martínez-Criado, M. H. Chu, S. Geburt, and C. Ronning, Nano Lett. **11**, 5322 (2011).

[20] T. Y. Ko, M.-H. Tsai, C.-S. Lee, and K. W. Sun, J. Nanopart. Res. **14**, 1253 (2012).

[21] R. D. Shannon and C. T. Prewitt, Acta Crystallogr., Sect. B **25**, 925 (1969).

[22] A. Smith, J.-F. Baumard, P. Abelard, and M.-F. Denanot, J. Appl. Phys. **65**, 5119 (1989).

[23] Ç. Kılıç, M. Aras, and S. Güler-Kılıç, Computational studies of bismuth-doped zinc oxide nanowires, in *Low-Dimensional and*

Nanostructured Materials and Devices: Properties, Synthesis, Characterization, Modelling and Applications, edited by H. Ünlü, M. N. J. Horing, and J. Dabowski (Springer International, Cham, Switzerland 2016), pp. 401–421.

[24] G. Kresse and J. Furthmüller, Phys. Rev. B **54**, 11169 (1996).

[25] G. Kresse and D. Joubert, Phys. Rev. B **59**, 1758 (1999).

[26] S. L. Dudarev, G. A. Botton, S. Y. Savrasov, C. J. Humphreys, and A. P. Sutton, Phys. Rev. B **57**, 1505 (1998).

[27] J. P. Perdew, K. Burke, and M. Ernzerhof, Phys. Rev. Lett. **77**, 3865 (1996).

[28] D. Hobbs, G. Kresse, and J. Hafner, Phys. Rev. B **62**, 11556 (2000).

[29] S. Steiner, S. Khmelevskyi, M. Marsmann, and G. Kresse, Phys. Rev. B **93**, 224425 (2016).

[30] M. Aras and Ç. Kılıç, J. Chem. Phys. **141**, 044106 (2014).

[31] P. J. Feibelman, Phys. Rev. B **64**, 125403 (2001).

[32] W. Fan, H. Xu, A. L. Rosa, T. Frauenheim, and R. Q. Zhang, Phys. Rev. B **76**, 073302 (2007).

[33] M. Yin, Y. Gu, I. L. Kuskovsky, T. Andelman, Y. Zhu, G. F. Neumark, and S. O'Brien, J. Am. Chem. Soc. **126**, 6206 (2004).

[34] D. Stichtenoth, C. Ronning, T. Niermann, L. Wischmeier, T. Voss, C.-J. Chien, P.-C. Chang, and J. G. Lu, Nanotechnology **18**, 435701 (2007).

[35] See Supplemental Material at http://link.aps.org/supplemental/10.1103/PhysRevB.97.035405 for the following: (i) Fig. S1 that displays the equilibrium atomic configuration for the ZnO:Bi nanowire under the applied electric fields, (ii) Table S1 that lists the electric-field-induced changes in the lengths of the bonds in Regions I and II depicted in Fig. 1(a), (iii) Fig. S2 that supplements Fig. 2, (vi) Fig. S3 displaying the electronic energy bands of the undoped ZnO nanowire for $\mathbf{E} = \mathbf{0}$ and $\mathbf{E} = 0.5\hat{\mathbf{x}}$ eV/Å, (v) Table S2 that lists the values for the magnitude and angles of the $\langle \mathbf{m} \rangle$ vectors depicted in Fig. 4(a), and (vi) Fig. S4 that displays the electronic energy bands of ZnO:Bi nanowires containing substitutional defects $Bi_{Zn}(s)$, $Bi_{Zn}(ss)$, and $Bi_{Zn}(b)$ for $\mathbf{E} = \mathbf{0}$, $0.5\hat{\mathbf{x}}$, and $0.5\hat{\mathbf{y}}$ eV/Å.

[36] Yu. A. Bychkov and É. I. Rashba, Pis'ma Zh. Eksp. Teor. Fiz. **39**, 66 (1984) [JETP Lett. **39**, 78 (1984)].

[37] K.-I. Kobayashi, O. Wada, M. Kobayashi, and Y. Takada, J. Am. Ceram. Soc. **81**, 2071 (1998).